PUBLISHED VERSION

Wendy S. L. Lee, Rajour T. Ako, Mei Xian Low, Madhu Bhaskaran, Sharath Sriram, Christophe Fumeaux, and Withawat Withayachumnankul

Dielectric-resonator metasurfaces for broadband terahertz quarter- and half-wave mirrors

http://hdl.handle.net/2440/113024

Dielectric-resonator metasurfaces for broadband terahertz quarter- and half-wave mirrors

WENDY S. L. LEE,[1,3] RAJOUR T. AKO,[2,3] MEI XIAN LOW,[2] MADHU BHASKARAN,[2] SHARATH SRIRAM,[2] CHRISTOPHE FUMEAUX,[1] AND WITHAWAT WITHAYACHUMNANKUL [1,*]

[1] School of Electrical and Electronic Engineering, The University of Adelaide, Adelaide, SA 5005, Australia
[2] Functional Materials and Microsystems Research and Micro Nano Research Facility, RMIT University, Melbourne, VIC 3001, Australia
[3] Equal contributions to this work
*withawat@adelaide.edu.au

Abstract: Polarization conversion of terahertz waves is important for applications in imaging and communications. Conventional wave plates used for polarization conversion are inherently bulky and operate at discrete wavelengths. As a substitute, we employ reflective metasurfaces composed of subwavelength resonators to obtain similar functionality but with enhanced performance. More specifically, we demonstrate low-order dielectric resonators in place of commonly used planar metallic resonators to achieve high radiation efficiencies. As a demonstration of the concept, we present firstly, a quarter-wave mirror that converts 45° incident linearly polarized waves into circularly polarized waves. Next, we present a half-wave mirror that preserves the handedness of circularly polarized waves upon reflection, and in addition, rotates linearly polarized waves by 90° upon reflection. Both metasurfaces operate with high efficiency over a measurable relative bandwidth of 49% for the quarter-wave mirror and 53% for the half-wave mirror. This broadband and high efficiency capabilities of our metasurfaces will allow to leverage maximum benefits from a vast terahertz bandwidth.

References and links

1. D. Grischkowsky, S. Keiding, M. van Exter, and C. Fattinger, "Far-infrared time-domain spectroscopy with terahertz beams of dielectrics and semiconductors," J. Opt. Soc. Am. B **7**, 2006–2015 (1990).
2. B. Scherger, M. Scheller, N. Vieweg, S. T. Cundiff, and M. Koch, "Paper terahertz wave plates," Opt. Express **19**, 24884–24889 (2011).
3. M. Reid and R. Fedosejevs, "Terahertz birefringence and attenuation properties of wood and paper," Appl. Opt. **45**, 2766–2772 (2006).
4. Z. Chen, Y. Gong, H. Dong, T. Notake, and H. Minamide, "Terahertz achromatic quarter wave plate: Design, fabrication, and characterization," Opt. Commun. **311**, 1–5 (2013).
5. J.-B. Masson and G. Gallot, "Terahertz achromatic quarter-wave plate," Opt. Lett. **31**, 265–267 (2006).
6. T. Niu, W. Withayachumnankul, A. Upadhyay, P. Gutruf, D. Abbott, M. Bhaskaran, S. Sriram, and C. Fumeaux, "Terahertz reflectarray as a polarizing beam splitter," Opt. Express **22**, 16148–16160 (2014).
7. T. Niu, A. Upadhyay, W. Withayachumnankul, D. Headland, D. Abbott, M. Bhaskaran, S. Sriram, and C. Fumeaux, "Polarization-dependent thin-film wire-grid reflectarray for terahertz waves," Appl. Phys. Lett. **107**, 031111 (2015).
8. J. Huang and J. A. Encinar, *Reflectarray antennas*, vol. 30 (John Wiley & Sons, 2007).
9. A. G. Lopez and H. G. Craighead, "Wave-plate polarizing beam splitter based on a form-birefringent multilayer grating," Opt. Lett. **23**, 1627–1629 (1998).
10. G. P. Nordin and P. C. Deguzman, "Broadband form birefringent quarter-wave plate for the mid-infrared wavelength region," Opt. Express **5**, 163–168 (1999).
11. R.-C. Tyan, P.-C. Sun, A. Scherer, and Y. Fainman, "Polarizing beam splitter based on the anisotropic spectral reflectivity characteristic of form-birefringent multilayer gratings," Opt. Lett. **21**, 761–763 (1996).
12. K. Takano, H. Yokoyama, A. Ichii, I. Morimoto, and M. Hangyo, "Wire-grid polarizer sheet in the terahertz region fabricated by nanoimprint technology," Opt. Lett. **36**, 2665–2667 (2011).

13. L. Sun, Z. Lü, D. Zhang, Z. Zhao, and J. Yuan, "Achromatic terahertz quarter-wave retarder in reflection mode," Appl. Phys. B **106**, 393–398 (2012).

14. W. Yu, A. Mizutani, H. Kikuta, and T. Konishi, "Reduced wavelength-dependent quarter-wave plate fabricated by a multilayered subwavelength structure," Appl. Opt. **45**, 2601–2606 (2006).

15. T. Suzuki, M. Nagai, and Y. Kishi, "Extreme-sensitivity terahertz polarizer inspired by an anisotropic cut-through metamaterial," Opt. Lett. **41**, 325–328 (2016).

16. Z. Han, S. Ohno, Y. Tokizane, K. Nawata, T. Notake, Y. Takida, and H. Minamide, "Thin terahertz-wave phase shifter by flexible film metamaterial with high transmission," Opt. Express **25**, 31186–31196 (2017).

17. M. Nagai, N. Mukai, Y. Minowa, M. Ashida, T. Suzuki, J. Takayanagi, and H. Ohtake, "Achromatic wave plate in thz frequency region based on parallel metal plate waveguides with a pillar array," Opt. Express **23**, 4641–4649 (2015).

18. W. Withayachumnankul and D. Abbott, "Metamaterials in the terahertz regime," IEEE Photonics J. **1**, 99–118 (2009).

19. N. I. Zheludev and Y. S. Kivshar, "From metamaterials to metadevices," Nat. Mater. **11**, 917–924 (2012).

20. A. Ebrahimi, S. Nirantar, W. Withayachumnankul, M. Bhaskaran, S. Sriram, S. F. Al-Sarawi, and D. Abbott, "Second-order terahertz bandpass frequency selective surface with miniaturized elements," IEEE Trans. Terahertz Sci. Technol. **5**, 761–769 (2015).

21. R. Singh, W. Cao, I. Al-Naib, L. Cong, W. Withayachumnankul, and W. Zhang, "Ultrasensitive terahertz sensing with high-q fano resonances in metasurfaces," Appl. Phys. Lett. **105**, 171101 (2014).

22. W. Withayachumnankul, H. Lin, K. Serita, C. M. Shah, S. Sriram, M. Bhaskaran, M. Tonouchi, C. Fumeaux, and D. Abbott, "Sub-diffraction thin-film sensing with planar terahertz metamaterials," Opt. Express **20**, 3345–3352 (2012).

23. Y. Z. Cheng, W. Withayachumnankul, A. Upadhyay, D. Headland, Y. Nie, R. Z. Gong, M. Bhaskaran, S. Sriram, and D. Abbott, "Ultrabroadband plasmonic absorber for terahertz waves," Adv. Opt. Mater. **3**, 376–380 (2015).

24. W. Withayachumnankul, C. M. Shah, C. Fumeaux, B. S.-Y. Ung, W. J. Padilla, M. Bhaskaran, D. Abbott, and S. Sriram, "Plasmonic resonance toward terahertz perfect absorbers," ACS Photon. **1**, 625–630 (2014).

25. J. E. Heyes, W. Withayachumnankul, N. K. Grady, D. R. Chowdhury, A. K. Azad, and H.-T. Chen, "Hybrid metasurface for ultra-broadband terahertz modulation," Appl. Phys. Lett. **105**, 181108 (2014).

26. W. S. L. Lee, S. Nirantar, D. Headland, M. Bhaskaran, S. Sriram, C. Fumeaux, and W. Withayachumnankul, "Broadband terahertz circular-polarization beam splitter," Adv. Opt. Mater. **3**, 1700852 (2018).

27. T. Niu, W. Withayachumnankul, B. S.-Y. Ung, H. Menekse, M. Bhaskaran, S. Sriram, and C. Fumeaux, "Experimental demonstration of reflectarray antennas at terahertz frequencies," Opt. Express **21**, 2875–2889 (2013).

28. N. Yu, P. Genevet, M. A. Kats, F. Aieta, J.-P. Tetienne, F. Capasso, and Z. Gaburro, "Light propagation with phase discontinuities: Generalized laws of reflection and refraction," Science **334**, 333–337 (2011).

29. P. Weis, O. Paul, C. Imhof, R. Beigang, and M. Rahm, "Strongly birefringent metamaterials as negative index terahertz wave plates," Appl. Phys. Lett. **95**, 171104 (2009).

30. C. Imhof and R. Zengerle, "Strong birefringence in left-handed metallic metamaterials," Opt. Commun. **280**, 213–216 (2007).

31. D. Wang, Y. Gu, Y. Gong, C.-W. Qiu, and M. Hong, "An ultrathin terahertz quarter-wave plate using planar babinet-inverted metasurface," Opt. Express **23**, 11114–11122 (2015).

32. A. C. Strikwerda, K. Fan, H. Tao, D. V. Pilon, X. Zhang, and R. D. Averitt, "Comparison of birefringent electric split-ring resonator and meanderline structures as quarter-wave plates at terahertz frequencies," Opt. Express **17**, 136–149 (2009).

33. N. K. Grady, J. E. Heyes, D. R. Chowdhury, Y. Zeng, M. T. Reiten, A. K. Azad, A. J. Taylor, D. A. R. Dalvit, and H.-T. Chen, "Terahertz metamaterials for linear polarization conversion and anomalous refraction," Science **340**, 1304–1307 (2013).

34. L. Cong, W. Cao, X. Zhang, Z. Tian, J. Gu, R. Singh, J. Han, and W. Zhang, "A perfect metamaterial polarization rotator," Appl. Phys. Lett. **103**, 171107 (2013).

35. W. Mo, X. Wei, K. Wang, Y. Li, and J. Liu, "Ultrathin flexible terahertz polarization converter based on metasurfaces," Opt. Express **24**, 13621–13627 (2016).

36. L. Cong, N. Xu, J. Gu, R. Singh, J. Han, and W. Zhang, "Highly flexible broadband terahertz metamaterial quarter-wave plate," Laser Photonics Rev. **8**, 626–632 (2014).

37. Y. Nakata, Y. Taira, T. Nakanishi, and F. Miyamaru, "Freestanding transparent terahertz half-wave plate using subwavelength cut-wire pairs," Opt. Express **25**, 2107–2114 (2017).

38. S. Ma, X. Wang, W. Luo, S. Sun, Y. Zhang, Q. He, and L. Zhou, "Ultra-wide band reflective metamaterial wave plates for terahertz waves," Eur. Lett. **117**, 37007 (2017).

39. Y. Z. Cheng, W. Withayachumnankul, A. Upadhyay, D. Headland, Y. Nie, R. Z. Gong, M. Bhaskaran, S. Sriram, and D. Abbott, "Ultrabroadband reflective polarization convertor for terahertz waves," Appl. Phys. Lett. **105**, 181111 (2014).

40. R. Xia, X. Jing, X. Gui, Y. Tian, and Z. Hong, "Broadband terahertz half-wave plate based on anisotropic polarization conversion metamaterials," Opt. Mater. Express **7**, 977–988 (2017).

41. J. B. Khurgin, "How to deal with the loss in plasmonics and metamaterials," Nature **10**, 2–6 (2015).

42. J. Zi, Q. Xu, Q. Wang, C. Tian, Y. Li, X. Zhang, J. Han, and W. Zhang, "Terahertz polarization converter based on all-dielectric high birefringence metamaterial with elliptical air holes," Opt. Commun. **416**, 130 – 136 (2018).

43. L. Zou, W. Withayachumnankul, C. M. Shah, A. Mitchell, M. Bhaskaran, S. Sriram, and C. Fumeaux, "Dielectric

resonator nanoantennas at visible frequencies," Opt. Express **21**, 1344–1352 (2013).

44. L. Zou, W. Withayachumnankul, C. M. Shah, A. Mitchell, M. Klemm, M. Bhaskaran, S. Sriram, and C. Fumeaux, "Efficiency and scalability of dielectric resonator antennas at optical frequencies," IEEE Photon. J **6**, 1–10 (2014).

45. W. S. L. Lee, K. Kaltenecker, S. Nirantar, W. Withayachumnankul, M. Walther, M. Bhaskaran, B. M. Fischer, S. Sriram, and C. Fumeaux, "Terahertz near-field imaging of dielectric resonators," Opt. Express **25**, 3756–3764 (2017).

46. D. Headland, E. Carrasco, S. Nirantar, W. Withayachumnankul, P. Gutruf, J. Schwarz, D. Abbott, M. Bhaskaran, S. Sriram, J. Perruisseau-Carrier, and C. Fumeaux, "Dielectric resonator reflectarray as high-efficiency nonuniform terahertz metasurface," ACS Photon. **3**, 1019–1026 (2016).

47. D. Headland, S. Nirantar, W. Withayachumnankul, P. Gutruf, D. Abbott, M. Bhaskaran, C. Fumeaux, and S. Sriram, "Terahertz magnetic mirror realized with dielectric resonator antennas," Adv. Mater. **27**, 7137–7144 (2015).

48. C. Qu, S. Ma, J. Hao, M. Qiu, X. Li, S. Xiao, Z. Miao, N. Dai, Q. He, S. Sun, and L. Zhou, "Tailor the functionalities of metasurfaces based on a complete phase diagram," Phys. Rev. Lett. **115**, 235503 (2015).

49. J. Dai, J. Zhang, W. Zhang, and D. Grischkowsky, "Terahertz time-domain spectroscopy characterization of the far-infrared absorption and index of refraction of high-resistivity, float-zone silicon," J. Opt. Soc. Am. B **21**, 1379–1386 (2004).

50. C. Balanis, *Antenna Theory: Analysis and Design* (Wiley, 1982).

51. J. Hao, Y. Yuan, L. Ran, T. Jiang, J. A. Kong, C. T. Chan, and L. Zhou, "Manipulating electromagnetic wave polarizations by anisotropic metamaterials," Phys. Rev. Lett. **99**, 063908 (2007).

1. Introduction

Polarization conversion is typically achieved by using wave plates made of birefringent materials. Specifically, as the wave propagates through such a material, orthogonal field components experience different refractive indices and thus different phase delays. A desired phase difference between the field components can be obtained by adjusting the material thickness. In the terahertz region, there is however a scarcity of naturally available birefringent materials with low absorption.

Some materials that exhibit birefringence in the terahertz region include crystalline dielectrics [1], paper [2] and wood [3]. Limitations of these natural materials include narrow-band operation, absorption and reflection losses, and device bulkiness. On top of that, paper and wood raise controllability and reliability issues. Stacked crystalline quarter-wave plates [4, 5] have been shown to overcome narrow bandwidth limitations, but however, they suffer from substantial device thickness and high cost. Additionally, the maximum measured transmission power for a stacked quarter-wave plate is merely 55% [5]. In order to overcome these limitations, periodic structures such as reflectarrays [6–8], gratings [9–13] and multilayered structures [9, 11, 14–17] can be employed to provide designable birefringence.

One alternative towards providing engineered birefringence at terahertz frequencies is to utilize metasurfaces. Metasurfaces, which are two-dimensional variants of metamaterials, open perspectives for novel devices due to their tailorable exotic properties not commonly found in nature [18, 19]. In principle, metasurfaces consist of periodically arranged subwavelength resonators that collectively yield controlled amplitude and phase responses. Through metasurface designs, fundamental properties of electromagnetic waves can be controlled, including phase, amplitude and polarization. A majority of previously proposed metasurfaces were made of metallic resonators, and demonstrated various functions including filters [20], sensors [21, 22], absorbers [23, 24], modulators [25], polarization beam splitters [6, 26] and beamformers [7, 27, 28].

Among the key components in terahertz systems that would benefit from broadband, designable birefringence are the quarter- and half-wave plate, which operate in transmission mode. Quarter-wave plates introduce a $\pi/2$ phase difference between the two orthogonal electric field components of an incident wave, while the amplitude responses are equal. This allows conversion between linearly polarized waves and circularly polarized waves. Several examples of planar quarter-wave plates made up of metallic resonators were demonstrated at terahertz frequencies [29–32]. Unlike quarter-wave plates, half-wave plates introduce a π phase difference between the two orthogonal field components. As a consequence, they can rotate 45° incident linearly polarized waves by 90°. At terahertz frequencies, half-wave plates made up of metallic resonators have also been

demonstrated [33–37]. A variant of wave plates that operate in reflection instead of transmission can be referred to as birefringent mirrors. For example, half-wave plates operate in transmission mode whereas birefringent half-wave mirrors have the same functionality but operate in reflection mode. At terahertz frequencies metallic resonators have been used to demonstrate broadband quarter-wave [38] and half-wave mirrors [38–40]. With metallic resonators, radiation efficiencies decrease with increasing frequencies due to Ohmic loss [41]. It is worth mentioning that periodic, elliptical air holes which causes anisotropy in dielectric material have also been shown to be efficient wave plates in the terahertz region [42].

A potential solution to overcome low radiation efficiencies of metallic resonators at higher frequencies is to incorporate dielectric resonators in metasurfaces. As the operation of dielectric resonators is based on resonant oscillations of displacement current, this alleviates Ohmic loss that metallic resonators suffer from. It has been demonstrated that dielectric-resonator-based metasurfaces are able to maintain high efficiencies across the microwave to visible frequency band [43, 44]. Furthermore, dielectric resonators are capable of supporting magnetic dipole resonances within a single dielectric layer as opposed to two layers as required by their metallic counterparts [45]. At terahertz frequencies, magnetic mirrors and reflectarrays based on dielectric resonators have been realized with high performance [46, 47]. It is also noteworthy that dielectric resonators exhibit a smoother phase variation as compared to their metallic counterparts. The phase gradient as a function of the frequency is dependent on the radiation quality factor of the resonators, Q_{rad}, where a higher value would result in a larger phase gradient. The lower Q_{rad} and thus smoother phase gradient of the dielectric resonators is due to their higher radiation loss or better coupling with free-space waves [48]. This feature benefits the polarization conversion purity of resulting waveplates and mirrors.

In this article, we present the design, fabrication and characterization of broadband quarter-wave and half-wave mirrors at terahertz frequencies. We employ dielectric resonators as building blocks of these mirrors in order to achieve high efficiency. Both these metasurfaces operate in reflection mode for 45° incidence angle. The geometry of these resonators is tailored for an ultra-wide operation bandwidth. Future applications in terahertz polarimetric devices and terahertz spectroscopy would benefit from these broadband planar metasurfaces. This article sequentially presents the quarter-wave mirror design and realization in Section 2, followed by the half-wave mirror design and realization in Section 3.

2. Quarter-wave mirror

2.1. Design

Figure 1 shows the unit cell design for the quarter-wave mirror. The resonators are made of instrinsic float-zone silicon of thickness 50 μm. This type of silicon has a moderate relative permittivity $\varepsilon_r = 11.68$ and negligible loss [49] at terahertz frequencies. Initially, the resonator was designed to be cross-shaped where the cross-arms were of different lengths. This cross geometry would resonate at different frequencies for the two orthogonal polarizations, thus leading to different phase responses. However, since curved edges are more compatible with micro-fabrication than sharp internal angles, the design was modified to incorporate sinusoidal sides. In order to avoid grating lobes, the largest dimension of the unit cell is chosen to be $l_{q1} = 70$ μm, which is less than half of the shortest operating wavelength of 171 μm at 1.75 THz. The ground plane of this metasurface is a gold layer with a thickness of 200 nm which is significantly above the skin depth at the frequency range of interest ($\approx$56 nm at 0.95 THz).

This structure is simulated using the frequency-domain solver in CST Microwave Studio with unit cell boundary conditions applied to the lateral boundaries. Floquet port excitations of either x- or y-polarized waves are used. The surface impedance accounting for metal loss in gold is used to model the thin gold metal layer in this simulation [27]. In order to recover the phase response induced solely by the resonator, the port is de-embedded to the ground plane. For functional
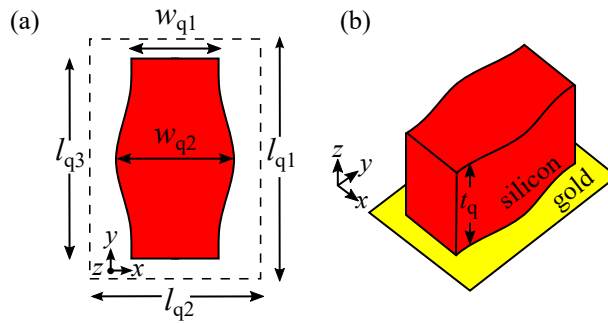
Fig. 1. Unit cell design of the quarter-wave mirror. (a) Top view and (b) 3D schematic of the unit cell. The side walls of the resonator are defined by a sine function with its peak and trough aligned with w_{q2} and w_{q1}, respectively. The dimensions are as follow: l_{q1} = 70 μm, l_{q2} = 50 μm, l_{q3} = 56 μm, w_{q1} = 25 μm, w_{q2} = 33 μm, t_q = 50 μm.

broadband quarter-wave mirrors, the phase difference between the x- and y-polarized electric field components in reflection is designed to be near $\pi/2$ radians across the frequency band of interest. The mechanism behind this feature will be detailed in Section 2.2.

2.2. Results and discussion

A section of the fabricated metasurface is shown in Fig. 2. The amplitude and phase responses in the major axes are evaluated. First, the sample is excited with vertically polarized waves (y-polarized) at 45° incidence in the xz plane and the detector measures the outgoing vertically polarized waves at the specular reflection angle. This set of measurement is then repeated for horizontally polarized (x-polarized) waves. For normalization of all measurements, a gold mirror is used in place of the sample.
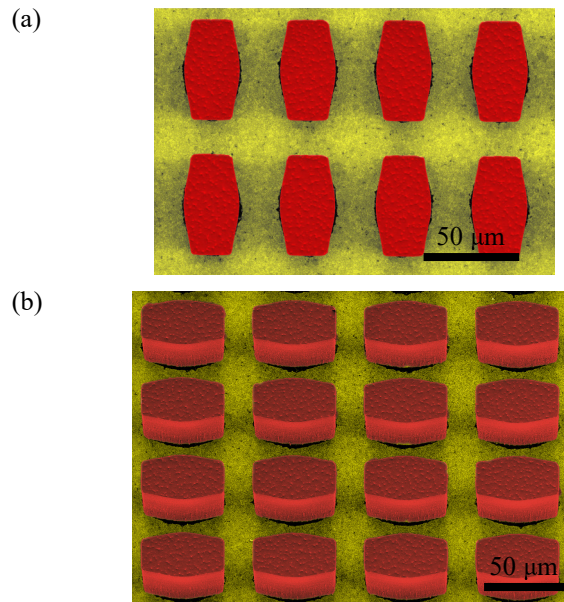

Fig. 2. Scanning electron micrographs showing a section of the fabricated quarter-wave mirror from a (a) top view and (b) isometric view.

The reflection phase responses of this metasurface for both polarizations are shown in Fig. 3(a) and the phase difference between the two orthogonal polarizations is shown in Fig. 3(b). The aforementioned results have been deembedded to the ground plane, so that the phase profile does not account for propagation in free space. It can be seen that the measured and simulated results are in good agreement with each other. A slight discrepancy in the phase results can be attributed to small misalignment of the gold mirror to obtain phase measurements in THz-TDS. As the detector is rotated to measure the orthogonal component of the terahertz wave, a slight error in phase and amplitude measurement also occurs. The phase profile for the measured results has been offset to match the simulation results to compensate a phase shift due to these misalignments. This phase offset is possible given the notable features in the sample phase profile. In order to illustrate the zero crossings that correspond to frequencies of resonance, the reflection phase response shown in the results are wrapped.

The phase response for the vertically polarized component approaches the zero crossing first, indicating that its fundamental resonance mode is at the lowest frequency. This is because of the larger size of the resonator in the y-dimension. The fundamental mode excited at the first
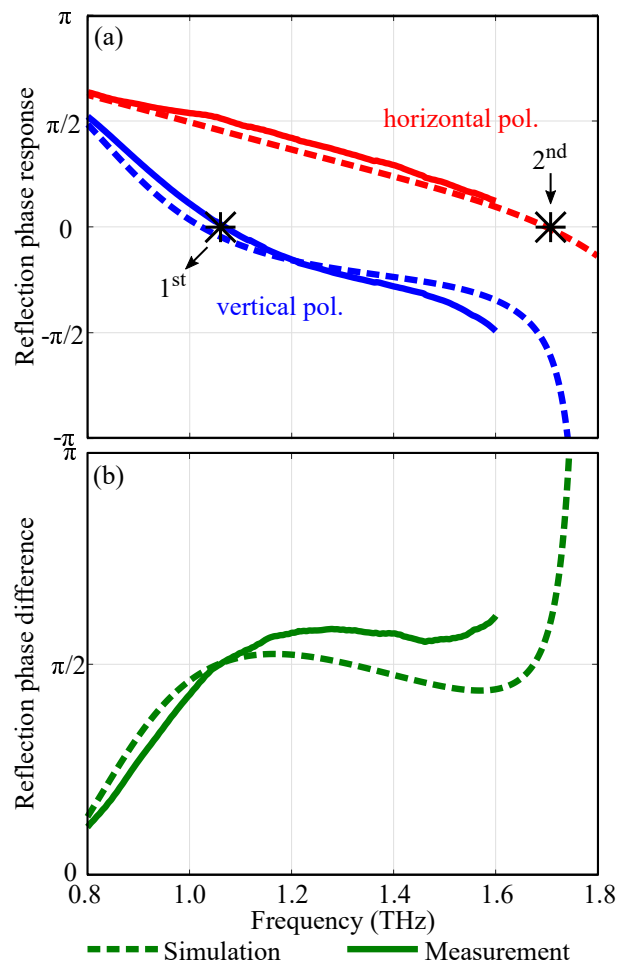

Fig. 3. Reflection phase profiles of the quarter-wave mirror. The reflection phase responses for the orthogonal polarizations are shown in (a) and their corresponding phase difference is shown in (b). The markers indicate the resonance modes in the quarter-wave mirror.
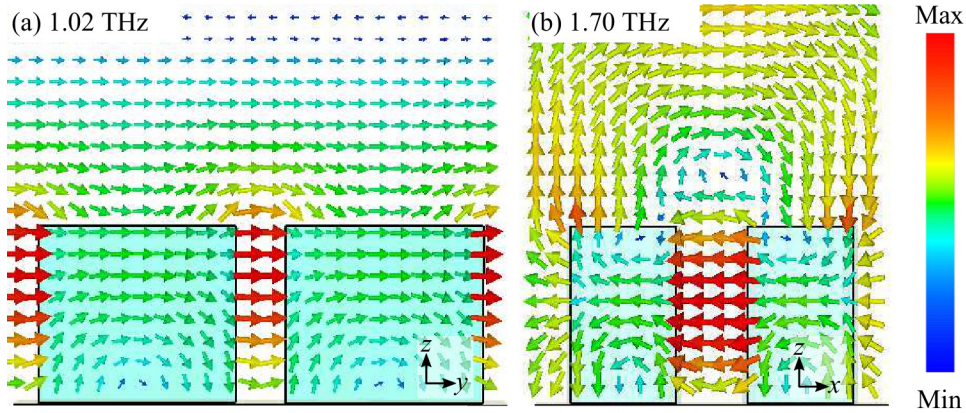
Fig. 4. Electric field distributions of the dielectric resonators in the quarter-wave mirror on resonance for (a) the y-polarization at 1.02 THz and (b) for the x-polarization at 1.70 THz where the wave is 45° incident in the xz plane. The rectangular boxes represent the resonators in their respective cut-plane view.

resonance is a magnetic dipole aligned with the x-axis. This mode of resonance corresponds to an electric field that loops within the resonator as shown in Fig. 4(a). Next, the horizontally polarized component approaches its resonance at a higher frequency of around 1.7 THz. For this second resonance, as shown in Fig. 4(b), the fundamental mode excited is a magnetic dipole, where a circulating electric field in the resonator is again clearly identified. As shown in Fig. 4(b), these two resonances allow for a continuing near $\pi/2$ phase difference between the two orthogonal polarizations from 0.97 – 1.60 THz. The simulated results shown in Fig. 3 indicate that the metasurface should be functional up to 1.75 THz. However, due to system limitations, experimental results beyond 1.60 THz are unreliable.

The measured reflection amplitudes for both polarizations are shown in Fig. 5. It can be seen that the metasurface is highly efficient, with measured average reflected amplitudes above 92% for the operating frequencies of 0.97 – 1.60 THz. The simulated reflection amplitudes are significantly higher than the measured results. This difference in amplitude can be attributed to tolerances in alignment, which results in apparent energy loss in the experiments. An existing terahertz quarter-wave mirror by Ma *et al.* [38] consisting of metallic resonators showed measured average reflected amplitudes of around 89% for the horizontal component and 74% for the vertical component at operating frequencies of 0.4 – 1.05 THz, corresponding to a bandwidth of 88%. Our design achieved markedly higher measured reflection amplitudes of greater than 92% for both orthogonal polarizations despite having a narrower bandwidth of 52% as compared to the 88% bandwidth achieved by Ma *et al.* Therefore, dielectric resonators are shown to have the potential to increase radiation efficiency as compared to their metallic counterparts.

The results suggest that the incident wave with its linear polarization at 45° can be converted into a circularly polarized wave upon reflection. In order to confirm that the reflected wave is circularly polarized, we calculate the axial ratio (AR) of its polarization ellipse. The AR is defined as ratio of the major axis to the minor axis [50], according to:

$$AR = \sqrt{\frac{E_{xo}^2 + E_{yo}^2 + \left[E_{xo}^4 + E_{yo}^4 + 2E_{xo}^2 E_{yo}^2 \cos(2\Delta\phi)\right]^{\frac{1}{2}}}{E_{xo}^2 + E_{yo}^2 - \left[E_{xo}^4 + E_{yo}^4 + 2E_{xo}^2 E_{yo}^2 \cos(2\Delta\phi)\right]^{\frac{1}{2}}}} \quad , \tag{1}$$

where E_{xo} and E_{yo} represent the reflection amplitudes for the horizontal and vertical polarizations
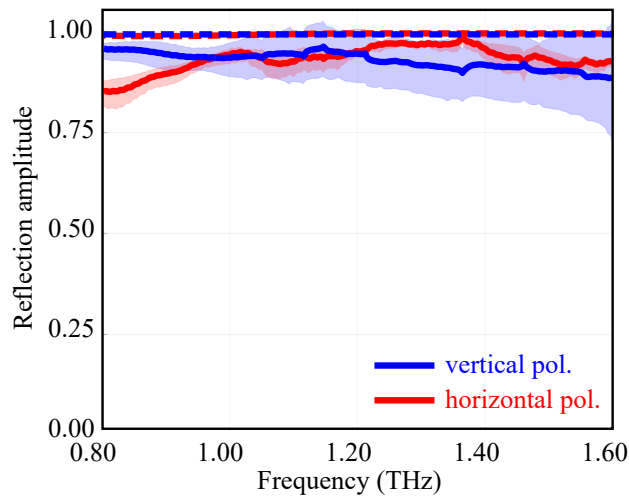
Fig. 5. Reflection amplitude profiles of the quarter-wave mirror. The dashed lines indicate the simulated results while the solid lines indicate the measured results. Error ranges due to experimental tolerances are indicated with shaded regions.

respectively while $\Delta\phi$ represents the phase difference between them. For ideal circular polarization, the AR should equal unity, or 0 dB. As shown in Fig. 6, the axial ratios of the simulated and measured results for our metasurface are in good agreement with each other. The axial ratio of the metasurface below the 3-dB threshold for circular polarization spans 0.97 THz – 1.60 THz, which is equivalent to a relative bandwidth of 49%. However, the relative bandwidth obtained in simulation is much higher, which is 58% for the frequency range of 0.94 – 1.71 THz. Thus, we can infer that upon excitation with a 45° linearly polarized wave, this metasurface functions as a broadband quarter-wave mirror which outputs a reflected circularly polarized wave.
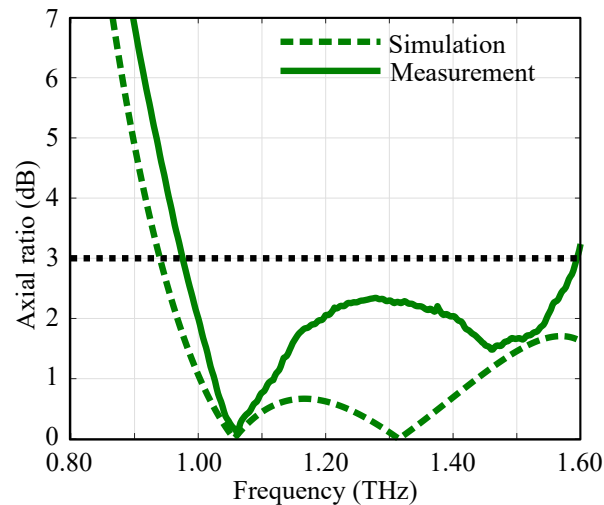

Fig. 6. Simulated and measured axial ratios of the quarter-wave mirror. The black dashed line marks the 3-dB threshold for circular polarization.

3. Half-wave mirror

3.1. Design

A similar design concept can be adapted to create a half-wave mirror. The initial unit cell design for the half-wave mirror is shown in Fig. 7(a). A dielectric resonator with sinusoidal edges is again made up of high-resistivity float-zone silicon on a 200 nm thick gold ground plane. For this design however, the height of the resonator is slightly reduced to 48 µm. The square unit cell is 76 µm in length, which is less than half the shortest operating wavelength of 176 µm at 1.70 THz to avoid grating lobes. A periodic repetition of this unit cell as shown in Fig. 7(a) in the x and y directions makes a reflective half-wave mirror. In this configuration, the resonators connect to form long, continuous bars in the y-dimension. This causes the structure to be very fragile due to the high mechanical stress at material interfaces between the continuous silicon bars and gold plate, particularly under temperature variations. As such, in the manufactured prototype, the continuous silicon bars of narrow width relative to long length (of 50 mm) developed stress cracks, causing delamination. In order to alleviate this mechanical stress, a gap of 6 µm is periodically introduced at every 14 unit cells.

The simulated reflection phase profiles for the original and modified designs are shown in Figs. 8(a) and 8(b) respectively. The original design refers to the design where the resonators connect to form long, continuous bars in the y-dimension whereas the modified design refers to the design where a gap of 6 µm is periodically introduced at every 14 unit cells. In general, the performance of the two designs are very similar. From either Figs. 8(a) and (b), we can infer three resonance modes from zero phase crossings, two of which for the vertical polarization and the other one for the horizontal polarization. These three resonances support a phase difference of close to π radians between the two orthogonal linearly polarized electric field components from 0.95 THz to 1.70 THz as shown in Fig. 8(c). It is noted that, with the introduction of a gap, as shown in Fig. 7(b), the positions of the three unique resonances do not shift, as indicated in Fig. 8(b). However, there are minimal fluctuations in the phase response for the vertically polarized component due to weak high-order resonances arising in the finite-length bars.
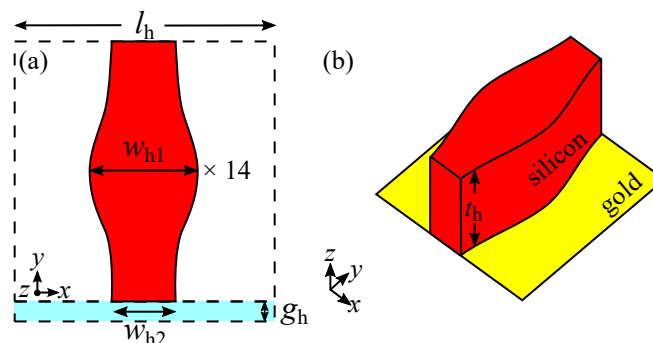

Fig. 7. Unit cell design of the half-wave mirror. (a) Unit cell design and (b) 3D schematic of the original unit cell design. The modified array design consists of 14 identical unit cells as shown in (a), followed by an extra gap of 6 µm as indicated by the shaded area. The dimensions are as follow: $l_h = 76$ µm, $w_{h1} = 30$ µm, $w_{h2} = 16$ µm, $g_h = 6$ µm, $t_h = 48$ µm.
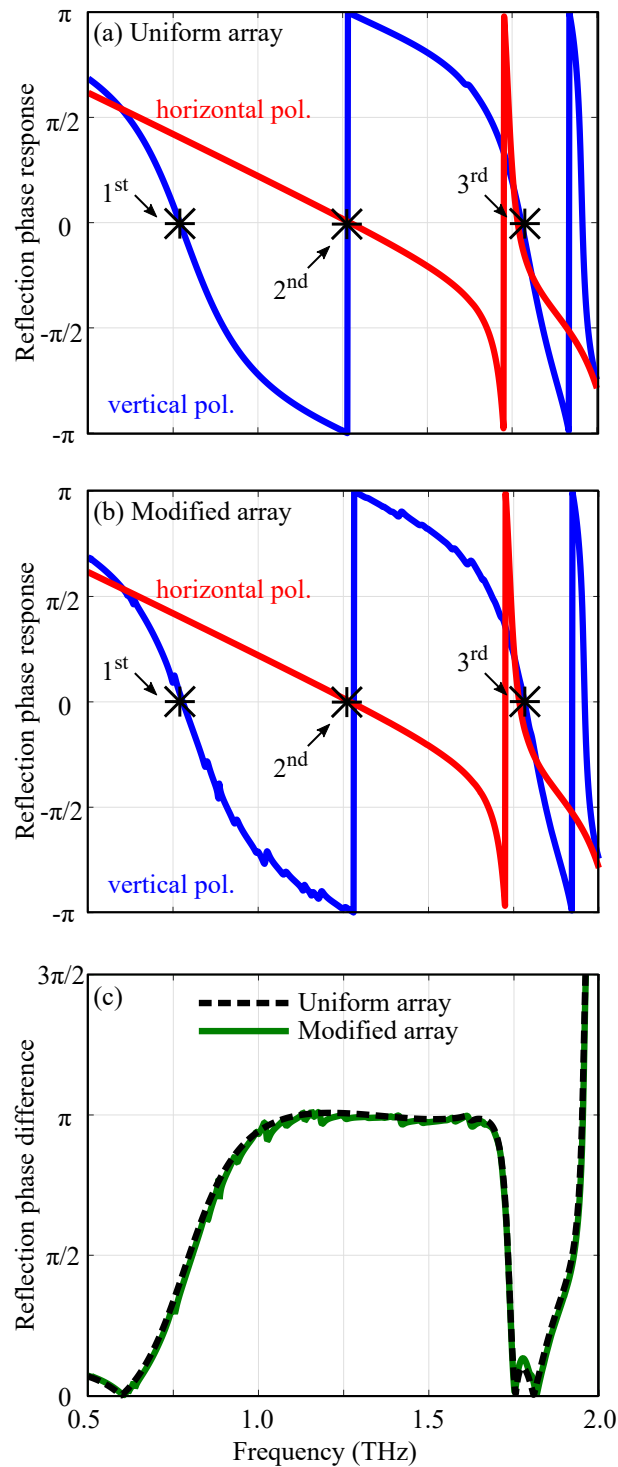
Fig. 8. Simulated reflection phase profiles of the half-wave mirrors. Reflection phase responses of the two orthogonal polarizations for the (a) original uniform array and (b) the modified array. (c) The reflection phase difference between the two orthogonal polarizations. The markers in (a) and (b) indicate resonance modes of the half-wave mirrors.

The mechanism of the three resonances is directly linked to the resonator geometry. Figure 9 shows the electric fields of the three resonances at their respective frequencies. Similar to the quarter-wave mirror, the phase response for the vertically polarized component approaches the zero crossing at the lower frequency, as the resonator is larger in the y-dimension. The first resonance is a magnetic dipole, as the electric fields oscillate in a loop, as shown in Fig. 9(a). Next, the phase response of the horizontally polarized component approaches the zero crossing on resonance. This resonance corresponds to a magnetic dipole, where the electric fields oscillate in a half-loop manner as shown in Fig. 9(b). After that, the phase response of the vertically polarized component approaches the zero crossing once again. The resonance mode of this third resonance is of a higher-order mode, where there exists two magnetic dipoles, which can be identified with circulating electric fields around the top and bottom of the resonator as shown in Fig. 9(c). The variation in the width of the resonator allows for the confinement and thus oscillation of displacement currents which support the excitation of both considered resonance modes for vertical polarization. Thus, the reflective near π phase difference is maintained, with minimal fluctuations as shown in Fig. 8(c).

3.2. Results and discussion

A portion of the manufactured half-wave mirror is shown in Fig. 10, where the gap between two long bars, each comprising 14 unit cells, is illustrated. For the validation experiment, the half-wave mirror is excited with a 45°-polarized wave at 45° incidence and the detector measures the outgoing specularly reflected waves. Two sets of measurements are taken where
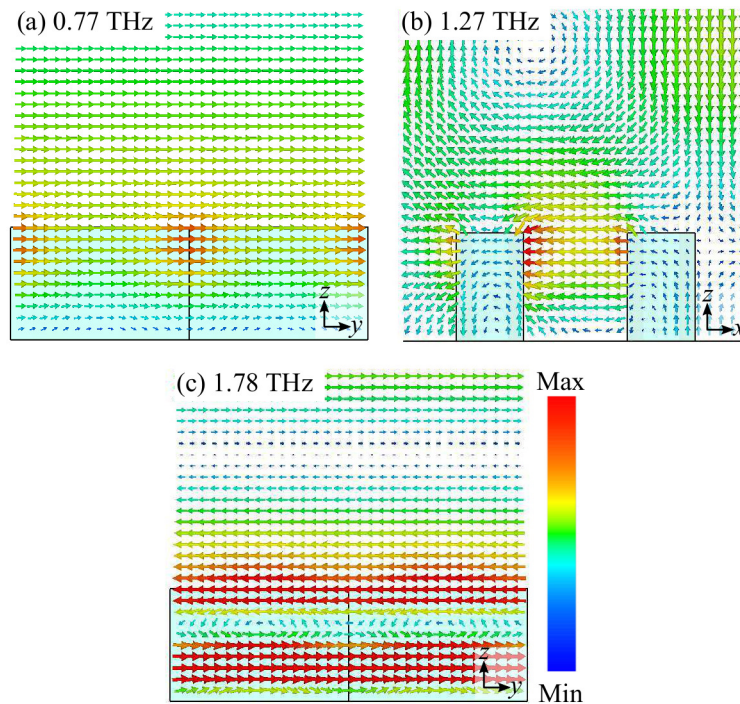

Fig. 9. Electric field distributions of the uniform dielectric resonator array of the half-wave mirror in their respective planes at the three resonances at (a) 0.77 THz, (b) 1.27 THz and (c) 1.78 THz. These figures are snapshots when the electric fields are at their maximum. The waves are y-polarized in (a-b) and x-polarized in (c) and the incident wave is at 45° in the xz plane. The rectangular boxes represent the resonators in their respective cut-plane view.
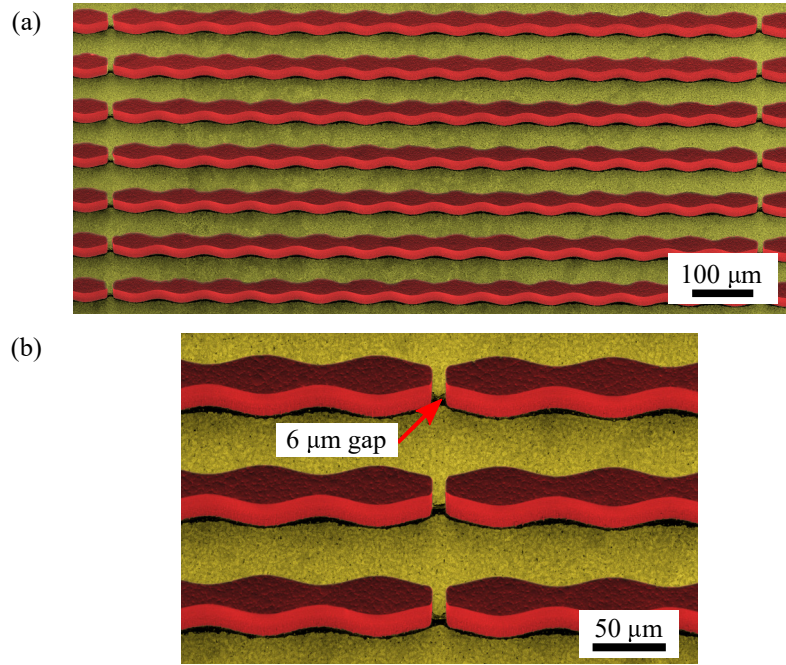
Fig. 10. Scanning electron micrographs of a section of the half-wave mirror at isometric views. Blocks of 14 unit cells are shown in (a) and a closed up of the gap, which is indicated by an arrow, is shown in (b).

the first set measures the co-polarization and the second set measures cross-polarization, which correspond to the reflected +45° and −45° polarized waves respectively. Figure 11 indicates that the simulated and measured results are in good agreement. From Fig. 11, it is observed that the cross-polarization amplitude is greater than 88%, with an average of 97% in simulation while the co-polarization amplitude is smaller than 31%, with an average around 9% for a frequency range of 0.79 – 1.58 THz. In measurement, the cross-polarization amplitude is greater than 72%, with an average of 79% while the co-polarization amplitude is smaller than 31%, with an average of 15% for a frequency range of 0.89 – 1.54 THz. Experimental tolerances including beam quality and system alignment contribute towards the missing energy in the measured co-polarization component. The slight shift in the frequency range of interest can be attributed to fabrication tolerances.

To determine the conversion efficiency of this half-wave mirror, we then proceed to calculate the polarization conversion ratio (PCR) [51] which is defined as:

$$\text{PCR} = \frac{|E_{\text{cr}}|^2}{|E_{\text{cr}}|^2 + |E_{\text{co}}|^2} \qquad (2)$$

where E_{cr} represents cross-polarized amplitude and E_{co} represents co-polarized amplitude. The PCR for the half-wave mirror is presented in Fig. 12, showing a relative bandwidth of 53% within the operating range of 0.89 THz – 1.54 THz. The relative bandwidth is defined to be the region where the PCR is above 90%. Similarly, the PCR obtained from simulation has a relative bandwidth of 66%, corresponding to a frequency range of 0.79 THz – 1.58 THz. An existing design by Cheng *et al.* [39] achieved a simulated relative bandwidth of 65%, corresponding to a frequency range of 0.72 THz – 1.41 THz. Ma *et al.* [38] demonstrates a metallic half-wave mirror with a relative bandwidth of 85%, corresponding to a frequency range of 0.40 THz –

0.99 THz. For the band where the PCR is greater than 90%, we calculate the PCR values for all three designs. Our design ultimately, achieves a markedly higher measured average polarization conversion efficiency of 96% as compared to 71% by Cheng *et al.* and 94% by Ma *et al.* Thus, polarization conversion mirrors consisting of dielectric resonators improve radiation efficiencies as compared to their metallic counterparts. The high value of conversion efficiency implies that our metasurface can rotate 45° incident linearly polarized waves by 90°. Additionally, in reflection, a half-wave mirror can preserve the handedness of circularly polarized waves.
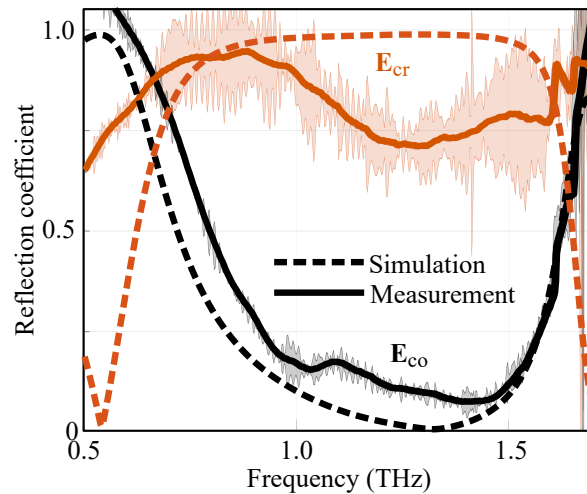

Fig. 11. Reflection amplitude profiles of the half-wave mirror at 45° incidence. E_{co} and E_{cr} correspond to the reflected +45° and −45° polarized waves respectively. The solid lines indicate measured results while the dashed lines indicate simulated results. Error ranges due to experimental tolerances are indicated with shaded regions.
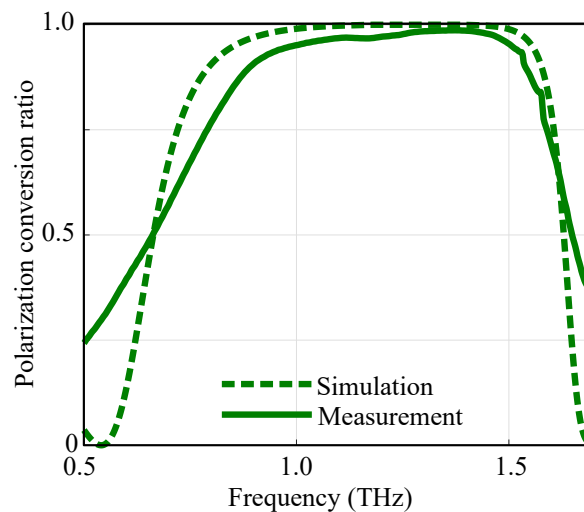

Fig. 12. Polarization conversion ratio of the half-wave mirror. This PCR is calculated from the amplitude responses in Fig. 11 by using Eq. 2.

4. Conclusion

In conclusion, we have demonstrated two broadband and highly efficient metasurfaces made up of dielectric resonators. These metasurfaces function as a quarter-wave and half-wave mirrors that operate in reflection. The quarter-wave mirror is capable of reflecting linearly polarized waves at 45° incidence into circularly polarized waves in a broadband range from 0.97 to 1.60 THz, or a relative bandwidth of 49% with high reflection efficiency. The half-wave mirror is capable of converting linearly polarized terahertz waves into its orthogonal polarized counterpart as well as preserving the handedness of circularly polarized waves upon reflection, in contrast to common mirrors. The average measured conversion efficiency of the half-wave mirror is 96% across the frequency range of 0.89 to 1.54 THz, corresponding to a relative bandwidth of 53%. The broadband capability of both metasurfaces is attributed to a combination of multiple resonances arising from the geometry of the resonators. Applications of terahertz polarimetry and spectroscopy would benefit from the proposed designs.

Appendix 1 - fabrication methods

Both quarter- and half-wave mirrors are fabricated using a similar procedure, but with different photomasks. Each mirror is composed of silicon resonators attached to a gold ground plane resting on another silicon substrate. Thus, each mirror requires two silicon wafers, a four inch double-polished <100> float-zone (FZ) silicon wafer of thickness 125 ± 25 μm and resistivity >5 kΩ-cm, and a three inch standard Si wafer. A 50 mm × 50 mm square section is diced (Dicing saw-DISCO DAD 321-NanoFab) out of the four inch silicon wafer. Both wafers are then cleaned with acetone, isopropyl alcohol (IPA) and H_2O, consecutively, for a minute, blow-dried with N_2 gun and dehydrated at 120°C for more than 5 minutes. In this work, the method of bonding used does not involve an SU_8 adhesion layer, contrary to our previous works [46, 47]. A gold-to-gold eutectic bonding is adopted to ensure high bonding strength that will be less affected by temperature changes. In this procedure, a 200 nm gold film is deposited on both wafers with a 20 nm Cr adhesion layer inside an electron beam evaporation chamber (PVD75, Kurt J. Lesker) at 0.5 As^{-1}, 4 $<10^{-7}$ Torr and at room temperature. After deposition, the 50 mm × 50 mm wafer is immediately placed onto the 3-inch silicon wafer using the gold-coated faces. Bonding is performed with the help of a wafer bonder (SB6 SUSS Microtech) at gold eutectic conditions. No special pre-treatment steps are required prior to bonding. Parameters such as the bonding force, bonding temperature, heating/cooling rate and pressure of chamber are sorted. For good bonding, the chamber was pumped down to a base pressure of $<5.0\times10^{-5}$ mbar and the temperature ramped up to 400 °C at 5 °C/min. Eutectic bonding commenced at 300 °C with an applied force of 2260 N including a 20 min dwelling time. All samples are left to cool slowly to room temperature. The bonded samples are then properly cleaned and dehydrated with standard microfabrication cleaning steps. Hereinafter, the fabrication procedure was as detailed in our previous work [46]. The float-zone silicon wafer of the bonded ensemble undergoes a thinning process to a height equal to that of the desired resonator, using a plasma-enhanced deep reactive ion etching. This is followed by patterning using standard photo-lithographic steps and subsequent silicon etching to the gold layer to realize desired resonators.

Appendix 2 - terahertz spectroscopy

A fiber-coupled terahertz time-domain spectroscopy is used in the experiment validation. The set-up used for the quarter-wave and half-wave mirrors is shown in Fig. 13. In these measurements, lenses with a focal length of 5 cm are used for beam collimation and focusing. Wire-grid polarizers are employed to ensure polarization purity. A focused, either vertically- or horizontally-polarized beam illuminates the sample at 45° incidence with a spot size around 1 mm. The sample then reflects the incident beam into the lenses which focuses the beam into the linearly polarized detector, which can be rotated for either vertically- or horizontally-polarized waves. For a Gaussian beam of waist of 1 mm, the corresponding Rayleigh range is 10 mm at a wavelength of 300 μm. As the focused Gaussian beam impinging on the sample is around the location of the beam waist, the beam can be assumed as having negligible angular divergence.
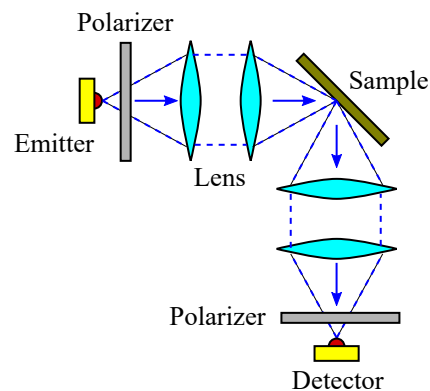

Fig. 13. Schematic of the experiment set-up.

Disclosures

The authors declare that there are no conflicts of interest related to this article.